

Article

Optimized Torque Performance of a 7-Phase Outer-Rotor Surface-Mounted Permanent Magnet Synchronous Machine for In-Wheel E-Motorcycle Application

Hamidreza Ghorbani ¹, Mohammadreza Moradian ^{1,2,*} and Mohamed Benbouzid ^{3,*}¹ Department of Electrical Engineering, Najafabad Branch, Islamic Azad University, Najafabad 8514143131, Iran² Smart Microgrid Research Center, Najafabad Branch, Islamic Azad University, Najafabad 8514143131, Iran³ Institut de Recherche Dupuy de Lôme (UMR CNRS 6027), University of Brest, 29238 Brest, France

* Correspondence: moradian@iaun.ac.ir (M.M.); mohamed.benbouzid@univ-brest.fr (M.B.)

Abstract: Four outer rotor surface-mounted permanent magnet synchronous machines (SPMSM), supplied by a seven-phase drive system, are proposed in this study, considering different q (number of stator slot per phase per pole ratio) to achieve a satisfying value of electromagnetic torque and Back-EMF with lower torque pulsation. Accordingly, the proposed configurations are investigated, and results are comparatively reported. Thus based on the results, the best-performing configuration, the candidate model, which presents the lowest torque pulsation with a desirable value of T_{avg} and Back-EMF is selected. In order to demonstrate the advantages of this candidate model, an optimization analysis is performed using 2D Finite Element Analysis (FEA). The resultant values of the variables are applied, designing three optimized models. Performance results of the optimized models demonstrate that T_{Cog} reduced noticeably and T_{Ripple} declined below 5%. The Artemis Drive-Cycles analysis results are also included for the best-optimized model, considering E-Motorcycle requirements and properties for urban, rural, and motorway driving conditions. Accordingly, in terms of In-Wheel application of the optimized machine, high torque/power density along with high values of PF and efficient performance are provided for E-Motorcycle application.

Keywords: Artemis Drive-Cycle; cogging torque; E-Motorcycle; optimization; SPMSM



Citation: Ghorbani, H.; Moradian, M.; Benbouzid, M. Optimized Torque Performance of a 7-Phase Outer-Rotor Surface-Mounted Permanent Magnet Synchronous Machine for In-Wheel E-Motorcycle Application. *Electronics* **2022**, *11*, 3192. <https://doi.org/10.3390/electronics11193192>

Academic Editor: Gianpaolo Vitale

Received: 6 September 2022

Accepted: 28 September 2022

Published: 5 October 2022

Publisher's Note: MDPI stays neutral with regard to jurisdictional claims in published maps and institutional affiliations.



Copyright: © 2022 by the authors. Licensee MDPI, Basel, Switzerland. This article is an open access article distributed under the terms and conditions of the Creative Commons Attribution (CC BY) license (<https://creativecommons.org/licenses/by/4.0/>).

1. Introduction

In terms of electric vehicle (EV) propulsion application, enormous studies have been conducted on transportation electrification technologies, requirements, policies, and electric machine topologies [1–4]. Permanent magnet synchronous machine (PMSM) is one of the major alternatives widely investigated for vehicular application [5–10]. PMSM topologies mostly benefit from a laminated cylindrical slotted stator with a 3-Phase winding, are supplied by an inverter set-up, and utilize a permanent magnet (PM) rotor. In comparison with induction machine (IM) technologies, PMSM provides advantages as outlined [4,5,11–14]: (i) higher power density, (ii) higher efficiency, (iii) high power factor, (iv) high ratio of output torque to weight and (v) more reliability. PMSM rotor structure is mainly introduced as interior/surface mounted PMSM (IPMSM and SPMSM respectively), located on the inner or outer side of the stator (IR or OR-SPMSM, respectively) [15,16]. Due to features of the external location of the rotor and corresponding high inertia, OR-SPMSM demonstrates constant speed operation rather than acceleration operation [4,10,15–17]. However, SPMSM machines suffer from high values of torque ripple, particularly when operating at low speed, and it is an urgent issue to be tackled which is studied in the majority of the literature considering topological design optimizations [12,16,18]. Optimizing the dimension of PMs and slot entrance designs, along with an optimal selection of slot/pole combinations for OR-SPMSM, has a high impact on the slotting effect and air-gap flux density of the machine

and hence effectively results in the cogging torque reduction. In addition, with the advent of power electronic converters, the multiphase drive system, with advantages such as reduction of torque pulsation and providing higher torque pulsation frequencies, can apply to electric motor drive systems [19–26]. Marmaras et al. [3] studied the behavior of the EV drivers and their impact on electricity and transport electrification systems. About 1000 EV agents have been investigated while being unaware/aware of the test. Consequently, it has been found that their behavior directly and indirectly affects both the road transport system and the electricity grid, traffic on the roads, the distribution network's stress and the usage of the charging-related infrastructure. Wu et al. [8] focus on design considerations of an OR-SPMSM with fractional concentrated winding configuration for In-Wheel applications, employing particle swarm optimization (PSO). Eight rotor pole numbers for a 48-slot stator are considered in this study. According to the applied PSO and 2D FEA results, the 48Slot/44Pole OR-SPMSM with about 10 Nm of torque ripple and 0.5 Nm of cogging torque provided the best performance in terms of EV application. A territory PSO (TPSO) is proposed by Ahn et al. [12] for design optimization of a SPMSM for unmanned aerial vehicle application (UAV). Accordingly, the torque performance of the proposed SPMSM model is reduced, whereas it has to be more precisely investigated because the model was applied to low-power SPMSM (below 0.5 kW). In addition, the optimum model still suffers from about 3% torque ripple for only 2.6 Nm of average torque. A numerical-based comparative analysis for OR brushless DC machine (BLDC) and SPMSM is studied by Lee et al. [15], as a low-voltage OR-BLDC and -SPMSM were analyzed using 3D FEA. The results demonstrated that the proposed OR-SPMSM presents lower value of torque fluctuations due to a reduction of stack length (torque ripple reduced by 78%) in comparison with the proposed OR-BLDC. Zhao et al. [16] designed and optimized an OR-SPMSM with reverse step shape PMs. Based on theoretical results, the air-gap flux harmonics decreased in comparison with the conventional SPMSM. Although, torque ripple value is reduced for the proposed OR-SPMSM, the optimized models a faced drop in torque density. Refs. [23,25] addresses the design of a 7-P SPMSM with tooth-concentrated winding using a maximum torque per ampere (MTPA) control strategy. Sculler [23] focused on the design of two radially magnetized PMs to reduce torque ripple. In addition, by injecting the fifth harmonic current, the produced torque can develop without increasing torque fluctuations. While Sculler et al. [25] investigated the simplicity and fault-tolerant ability of a 7-phase SPMSM.

Therefore, to study tackling the high values of torque ripple in a SPMSM, this paper aims to investigate an OR-SPMSM supplied by a 7-phase drive system with four winding configurations, particularly for low torque ripple In-Wheel E-Motorcycle application. Results are comparatively reported and the best-performing configuration, providing a desirable amount of torque density with low fluctuations, is selected to be precisely studied. Hence, to aim for this goal and for clearing the strengths of the machine, a 2D FEA is applied to 1000 structural designs considering the best-performed winding pattern. The final optimized models, meeting the objective function constraints, are determined and results have been compared. Finally, the model presenting the best performance is analyzed under the standard Artemis Drive Cycle test and results reported for urban, road, and motorway operation. Accordingly, the optimized OR-SPMSM presents high torque density with at most 135 mm outer diameter, which makes it suitable to be placed in motorcycle wheels of an average size as specified in Section 4.5, in which the constraints for practically utilizing the proposed optimized model are discussed and studied. Other constraints about such application are also listed and theoretical principle is discussed. Moreover, the operating outputs for such applications are reported, including avg. and max. operating speeds, losses, in-output energies and operational efficiencies.

2. System Equations Review

In the following sections, summarized design formulation and performance equations for multi-phase PM machines and proposed models are presented.

2.1. Multiphase PM-Machine Equations

Generally, for any multi-phase electrical machine, power, P_e , and torque, T_e , can be expressed as [27]:

$$P_e = \frac{m}{T} \int_0^T e(t)i(t)dt \quad (1)$$

$$T_e = \frac{P_e}{\Omega} = \frac{m}{\Omega T} \int_0^T e(t)i(t)dt \quad (2)$$

where Ω is the rotational angular speed, m is the number of phases, T is the cycle period of Back-EMF, $e(t)$ and $i(t)$ are one phase Back-EMF and current, respectively. To enhance torque density in the m -phase system, current harmonic orders less than m can be injected into the system [19,27]. Hence, assuming the same harmonic orders for Back-EMF [27]:

$$e(t) = \sum_v^{m-2} E_v \sin(v\omega t) \quad (3)$$

$$i(t) = \sum_{\kappa=1}^{m-2} I_{\kappa} \sin(\kappa\omega t) \quad (4)$$

where E_v and I_{κ} are v th and κ th harmonic peak values of Back-EMF and current, respectively, and ω is the electrical angular frequency. Accordingly, the torque equation can be rewritten as [27]:

$$T_e = \sum_{\kappa=1}^{m-2} \frac{m}{2\Omega} E_{\kappa} I_{\kappa} \quad (5)$$

and E_{κ} , the peak value of Back-EMF is given by:

$$E_{\kappa} = \Omega K_{e\kappa} B_{\kappa} N_t D_g L \quad (6)$$

where κ th harmonic of winding factor and air-gap flux density are $K_{e\kappa}$ and B_{κ} , respectively. N_t is the number of turns per phase and D_g and L are the air-gap diameter and stack length of the machine, respectively. In order to achieve torque enhancements, the RMS value of phase current (including peak values of current harmonics) can be given as [27]:

$$I_{rms} = \frac{I_1}{\sqrt{2}K_{e1}B_1} \sqrt{\sum_{\kappa=1}^{m-2} (K_{e\kappa}B_{\kappa})^2} \quad (7)$$

where I_1 is the peak value of 1st current harmonic, K_{e1} and B_1 are the corresponding winding factor and air-gap flux density harmonics, respectively. Inserting electrical loading, A , as [27]:

$$A = 2mN_t \frac{I_{rms}}{\pi D_g} \quad (8)$$

into (7), one can obtain:

$$I_1 = \frac{\pi A D_g K_{e1} B_1}{\sqrt{2} m N_t \sqrt{\sum_{\kappa=1}^{m-2} (K_{e\kappa} B_{\kappa})^2}} \quad (9)$$

and

$$I_{\kappa} = \frac{K_{e\kappa} B_{\kappa}}{K_{e1} B_1} I_1 \quad (10)$$

Thus, the electromagnetic torque can be expressed as [25]:

$$T_e = \frac{\pi A D_g^2 L}{2\sqrt{2}} \sum_{v=1}^{m-2} \frac{(K_{ev} B_v)^2}{\sqrt{\sum_{\kappa=1}^{m-2} (K_{e\kappa} B_{\kappa})^2}} \quad (11)$$

Calculating D_o , outer diameter, by

$$\lambda_o = \frac{D_g}{D_o} \tag{12}$$

Torque equation based on sizing equation, D_o^2L , for a multiphase PM machine can be expressed as Equation (13):

$$T_e = \frac{\pi A \lambda_o D_o^2 L}{2\sqrt{2}} \sum_{v=1}^{m-2} \frac{(K_{ev} B_v)^2}{\sqrt{\sum_{\kappa=1}^{m-2} (K_{e\kappa} B_\kappa)^2}} \tag{13}$$

2.2. Winding Types

Considering the value of q , the number of stator slots per rotor pole per phase, two main types of winding can be introduced [28,29]:

- (i) q is an integer, distributed-winding type: conventionally used in electric machines, where greater value of q results in more sinusoidal magnetomotive force (MMF) wave produced.
- (ii) q is not an integer, concentrated-winding type: this type is mostly wound in single or double layers, for which the comparison is given in Table 1.

Table 1. Concentrated Single- and Double-layer winding Properties [29].

Winding Layers	Single	Double
Fundamental winding factor (k_w)	high	low
End Windings	long	short
Eddy Current	high	low
Over-load Torque Capability	high	low
Back-EMF Harmonics	high	low
Torque Ripple (T_{Ripple})	high	low

It can be found from Equation (13) that the variation in air-gap flux density and the value of m has a high impact on the torque performance of the machine. In addition, based on the q ratio as:

$$q = \frac{N_s}{mN_p} \tag{14}$$

the values of N_s , N_p , and m have a direct effect on the winding pattern, corresponding winding factor and MMF. Overall, B_g is influenced by the ratio of slot/pole combination along with the number of phases and the value of PMs flux linkage in the rotor. Therefore, it directly affects the electromagnetic torque of the PM machine.

3. Proposed Model

In this study, based on the former introduction in Section 2, four winding patterns and corresponding N_s for a six-pole seven-phase outer-rotor SPM machine (Figure 1) are investigated for In-Wheel application in an E-Motorcycle. The proposed models are designed and analyzed under the same condition, assuming 40 °C of ambient temperature.

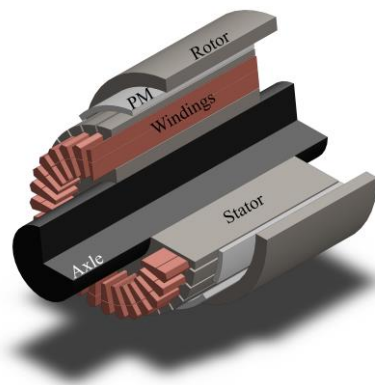


Figure 1. 3D-View of an OR-SPMSM.

3.1. Configuration and Design Parameters

Four N_s/N_p ratios, namely 42/6, 28/6, 21/6, and 14/6, are considered in this study, resulting in q equal to 1, 2/3, 1/2, and 1/3, respectively. The initial values of design parameters are given in Table 2. The winding patterns and the objective function of this study are as follow.

Table 2. Initial Design Parameters.

Quantity	Sym.	Value	Unit
Num. Phases	m	7	—
Rated Voltage	V_n	120	V
Rated Current	I_n	70	A
Rated Speed	n_r	1500	rpm
Motor Length	L_M	100	mm
Stator Outer Diameter	D_{SO}	135	mm
Stator Slot Depth	L_{SSD}	25	mm
Rotor Outer Diameter	D_{RO}	165	mm
Rotor Back Iron	D_{RBI}	10	mm
Axle Diameter	D_A	55	mm
Num. Stator Slots	N_s	42, 28, 21, 14	—
Num. Rotor Poles	N_p	6	—
Ratios of N_s/mN_p	q	1, 2/3, 1/2, 1/3	—
Air-gap Length	L_g	1	mm
Stator Tooth Width	W_{ST}	5	mm
Stator Slot Opening	L_{SO}	2	mm
Stator Tooth Tip Depth	L_{TTD}	1	mm
PM Length	L_{PM}	50	°
PM Thickness	W_{PM}	4	mm
PM Type	—	N42SH	—
Steel Type	—	M400-50A	—

3.2. Winding Pattern

According to the value of q in Table 2, four concentrated winding patterns and selected N_s values as shown in Figures 2–5 are considered. The corresponding winding factor and winding harmonics of each q are presented in Figures 6 and 7, respectively.

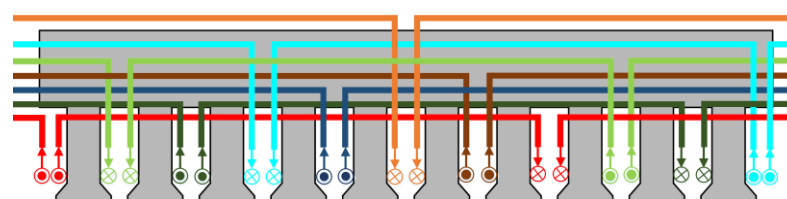


Figure 2. Winding pattern for $N_p = 6, N_s = 42 (q = 1)$.

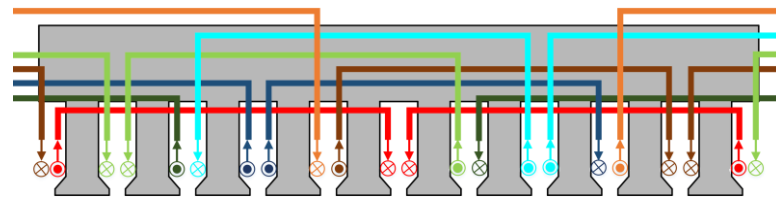


Figure 3. Winding pattern for $N_p = 6, N_s = 28 (q = 2/3)$.

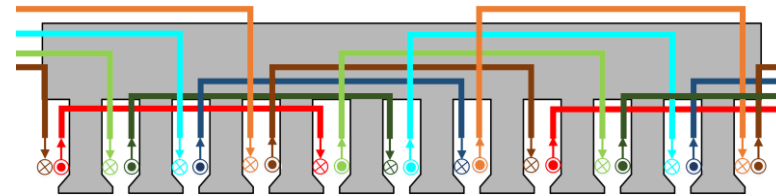


Figure 4. Winding pattern for $N_p = 6, N_s = 21 (q = 1/2)$.

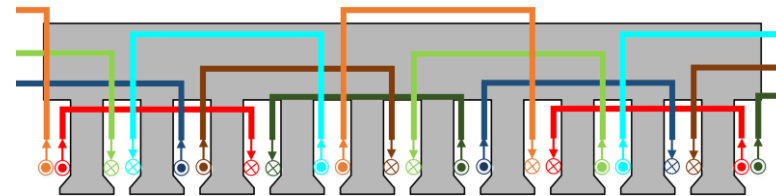


Figure 5. Winding pattern for $N_p = 6, N_s = 14 (q = 1/3)$.

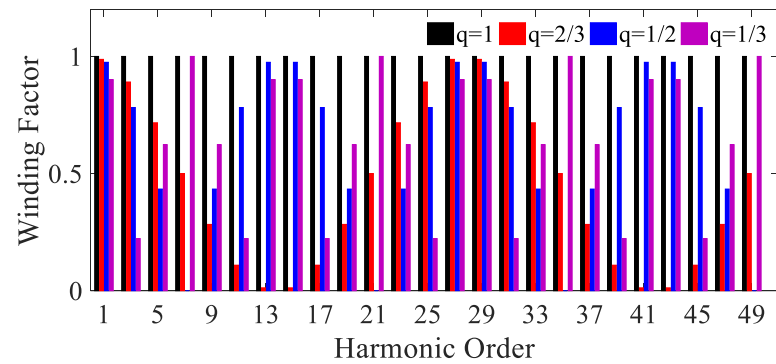


Figure 6. Winding factor.

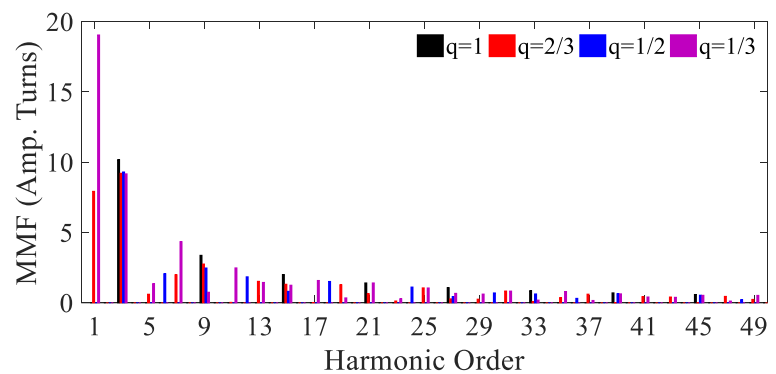


Figure 7. Winding harmonics.

3.3. Variables and Objective Function

The objective function of this study is to enhance torque performance of the machine for electric vehicle application. Accordingly, the following development processes are considered to be investigated using 2D Finite Element Analysis (FEA). The initial design

parameters are presented in Table 2, and the variables considered for sensitivity analysis of the candidate model are illustrated in Figure 8.

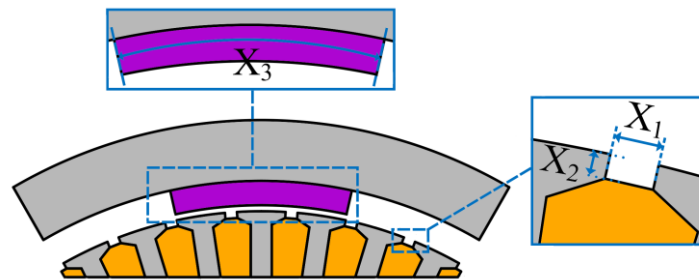


Figure 8. Variables of sensitivity analysis.

- ❖ Initial Configurations
 - Objective Function: minimum torque pulsation, satisfying torque density and Back-EMF: determination through q selection
 - Constraints: initial design parameters in Table 2.
- ❖ Candidate Model
 - Objective Function: minimize torque pulsation and maximize torque: for determination of the best-performing model through FE sensitivity analysis
 - Constraints: $W_{PM} = 4$ mm, $L_{SSD} = 25$ mm, $W_{ST} = 5$ mm, $T_{Cog} \leq 1$ Nm, $T_{Ripple} < 5\%$, $T_{avg} \geq 80$ Nm
- ❖ PM Dimension and slot entrance design variables: 0 mm $\leq X_1 \leq 9$ mm, 0 mm $\leq X_2 \leq 5$ mm, $5^\circ \leq X_3 \leq 55^\circ$

4. E-Magnetic Results

By applying 2D FEA to the proposed structures, the following results have been achieved, so that in Section 4.1, initial models are investigated in order to select the candidate model, which provides a satisfying and desirable amount of torque and Back-EMF amplitude. Then the resultant candidate model is sensitively analyzed with constraints mentioned for X_1 , X_2 , and X_3 , with results illustrated in Section 4.2. Optimized models, providing highest T_{avg} , lowest T_{Cog} and T_{Ripple} are introduced in Section 4.3, where comparative results are reported. In Section 4.4 efficiency and power factor maps of the best-optimized model are reported. Finally, Section 4.5 displays results of Drive-Cycle torque graph for In-Wheel application of an E-Motorcycle, adopting the best-performing model.

4.1. Analysis of the Initial Models

Figures 9–12 demonstrate the analysis results of the average torque, cogging torque, torque ripple, and back-EMF for the initial configurations, respectively.

As shown in Figure 9a, the greater the value of q , the more average torque is produced by the proposed 7-P SPMSM. As a result, according to torque FFT analysis shown in Figure 9b, the amplitude of the fundamental harmonic increases as q grows.

Based on T_{Cog} results, illustrated in Figure 10, the cogging torque does not follow the same path the average torque did, thus, the growing value of q does not directly affect T_{Cog} . This means, for $q = 2/3$ and $1/3$, the peak-to-peak cogging torque is approximately 50% less than $q = 1$ and $1/2$, respectively, where $q = 2/3$ presents the lowest T_{Cog} (less than 2 Nm).

On the contrary, T_{Ripple} is reduced for $q \leq 2/3$, reaching from 13% in $q = 1/3$ to 7% in $q = 2/3$; however, it is suddenly doubled in $q = 1$ (Figure 11).

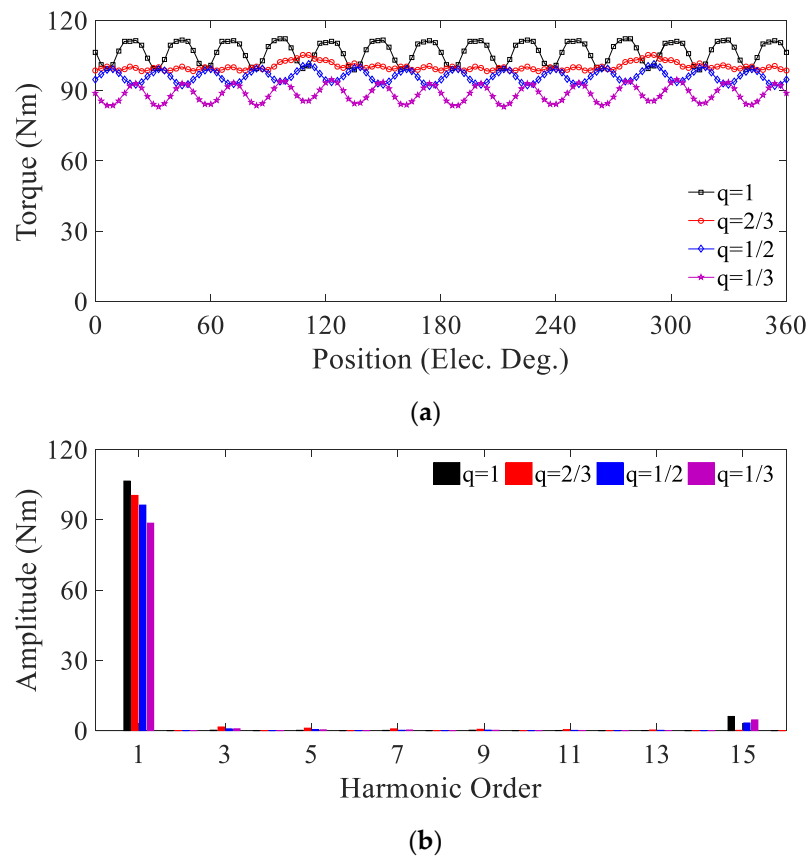


Figure 9. Initial models: (a) Average torque, (b) Torque FFT analysis.

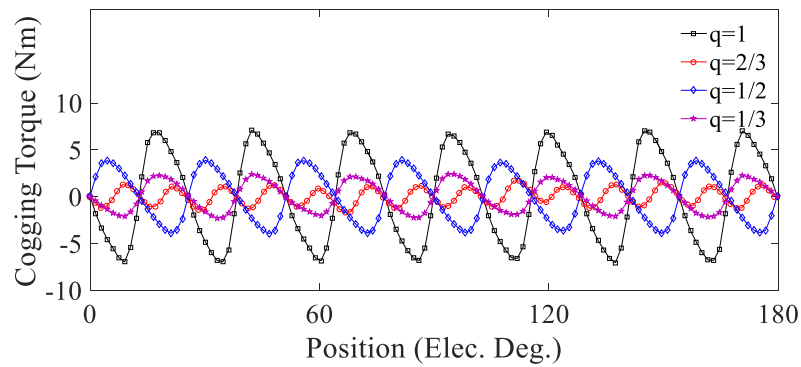


Figure 10. Cogging torque of the initial models.

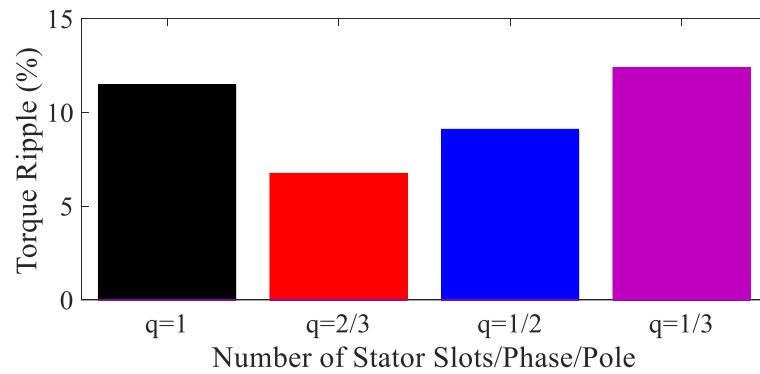


Figure 11. Torque ripple of the initial models.

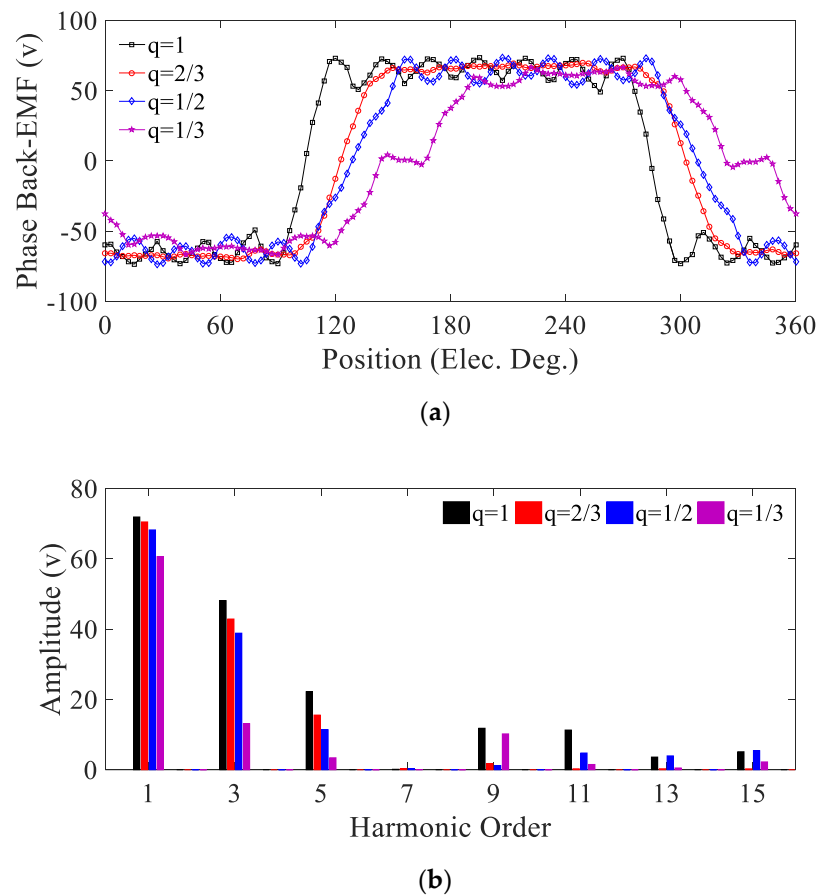


Figure 12. Initial models: (a) Phase Back-EMF, (b) Back-EMF FFT.

The one-phase back-EMF and the corresponding FFT analysis results of the proposed models are presented in Figure 12a,b, respectively. Accordingly, the peak value of the phase back-EMF increased along with the increasing value of q , from 50 V to 70 V for $q = 1/3$ to $q = 1$, respectively. The amplitude of harmonics for $q = 2/3$ continuously decreased to about zero for $n \geq 7$ th harmonic, whereas other q values suffer from $n > 7$ harmonic orders. Thus, the phase back-EMF, produced by the $q = 2/3$ model, presents fewer fluctuations with desirable peak values.

Based on results discussed and demonstrated in Figures 9–12, the proposed 28/6 initial model with $q = 2/3$ provides a satisfying average torque value of 95 Nm, T_{Cog} less than 2 Nm, 7% of T_{Ripple} and 67 V of phase back-EMF, and is selected as the candidate model. Hence, in order to achieve the goal of this study, reduction of torque pulsation, a sensitivity analysis is performed considering the variables shown in Figure 8. The flux density distribution of the initial models is illustrated in Appendix A.

4.2. Sensitivity Analysis of the Candidate Model

As depicted in Figure 8, the analysis variables, namely X_1 , X_2 , and X_3 , are sensitively analyzed for the candidate model from Section 4.1, considering the constraints in the objective function. Torque, cogging torque, and torque ripple results of this sensitivity analysis are illustrated in Figures 13–15. As depicted in Figure 13, decreasing value of X_1 and X_2 along with an increase in X_3 value increases T_{avg} , so that $T_{avg-Max}$ produced equals 96.2 Nm for $X_1 = 2.5$ mm, $X_2 = 3.5$ mm, and $X_3 = 45^\circ$. T_{Cog} results are illustrated in Figure 14, where X_1 and X_2 should move in opposite directions in order to provide lower cogging torque. For X_3 , T_{Cog} fluctuates in the way that the lowest T_{Cog} produced is 0.018 Nm as $X_1 = 0$ mm, $X_2 = 5$ mm and $X_3 = 5^\circ$. Lower T_{Ripple} is presented by increasing values of X_2 and X_3 , where X_1 causes fluctuations in torque ripple. However, $T_{Ripple-Min}$ is provided by values of $X_1 = 0$ mm, $X_2 = 4.5$ mm and $X_3 = 45^\circ$, which equal to 1.7%. Based on

the results shown in Figures 13–15, and resultant values for X_1 to X_3 , the best-performing models are categorized. They are those which provide maximum average torque (Model-I), minimum cogging torque (Model-II), and minimum torque ripple (Model-III), respectively. Corresponding results for the optimized models are reported in Table 3.

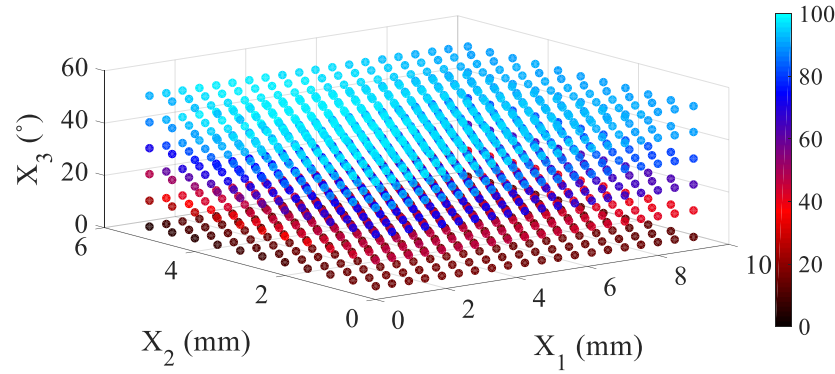


Figure 13. T_{avg} (Nm) vs. X_1 vs. X_2 vs. X_3 .

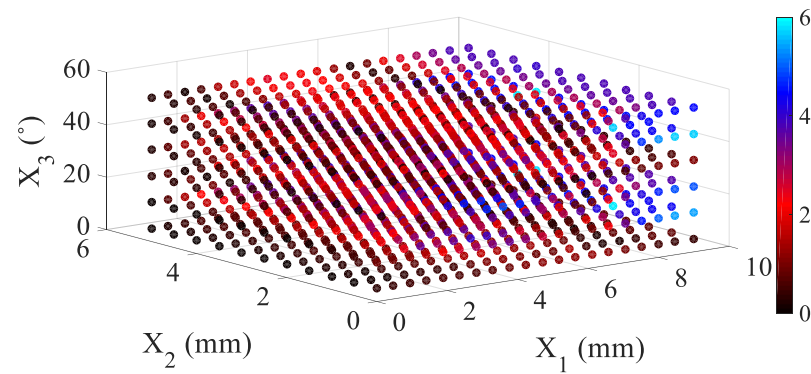


Figure 14. T_{Cog} (Nm) vs. X_1 vs. X_2 vs. X_3 .

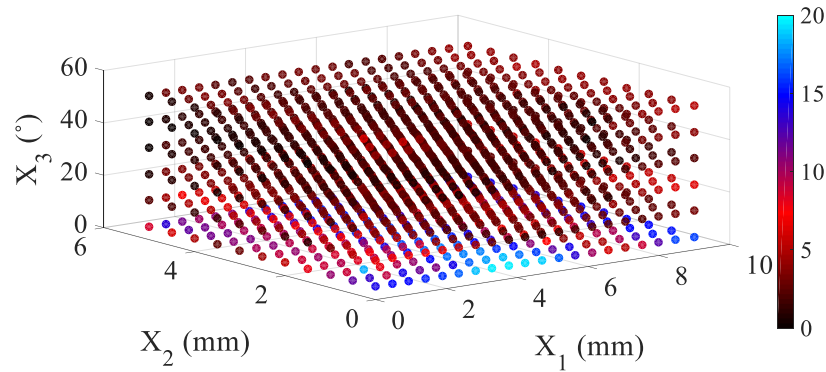


Figure 15. T_{Ripple} (%) vs. X_1 vs. X_2 vs. X_3 .

Table 3. Output Data of the Optimized Models.

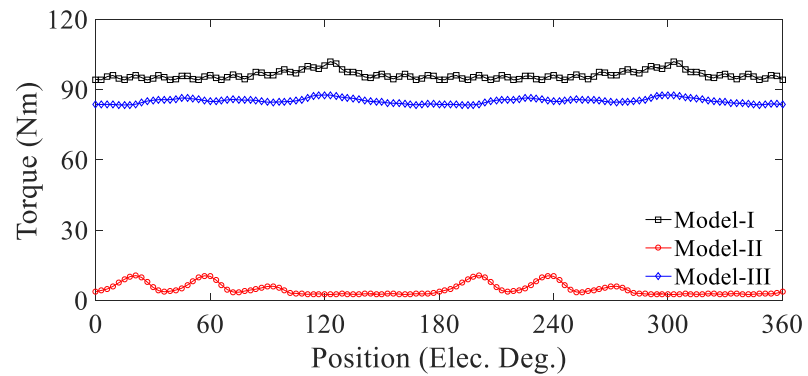
Parameter	Model-I	Model-II	Model-III
X_1 (mm)	2.5	0	0
X_2 (mm)	3	5	4.5
X_3 (°)	45	5	45
T_{Avg} (Nm)	96.2	4.73	85.1
T_{Cog} (Nm)	8.5	0.018	0.26
T_{Ripple} (%)	7.8	8.53	1.7

Table 3. Cont.

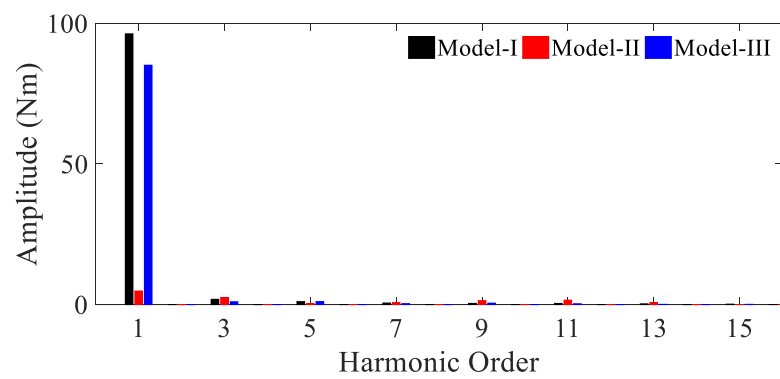
Parameter	Model-I	Model-II	Model-III
Eff. (%)	88.5	22.94	86.75
PF	0.9	0.18	0.82
B-EMF (V)	114.7	8.2	67.2

4.3. Analysis of the Optimized Models

With regard to the goal of this paper, a comparative study is performed for the models designed by means of X values in Table 3, and the results are presented in Figures 16–19.



(a)



(b)

Figure 16. Optimized models:(a) Average torque, (b) Torque FFT.

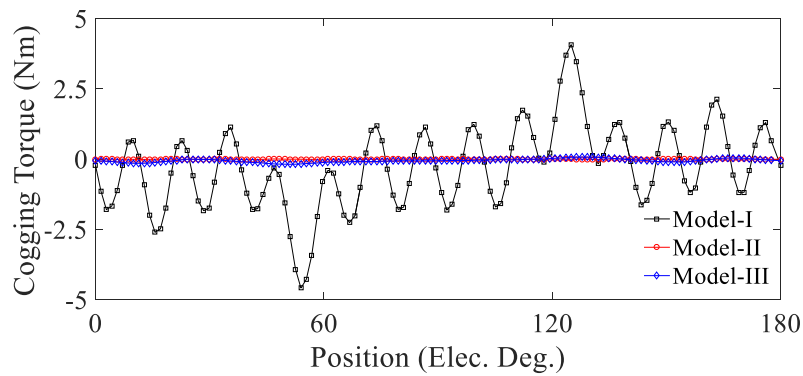


Figure 17. Cogging torque of the optimized models.

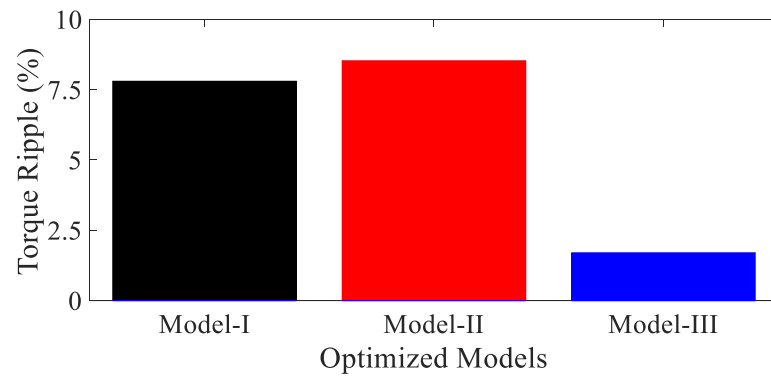
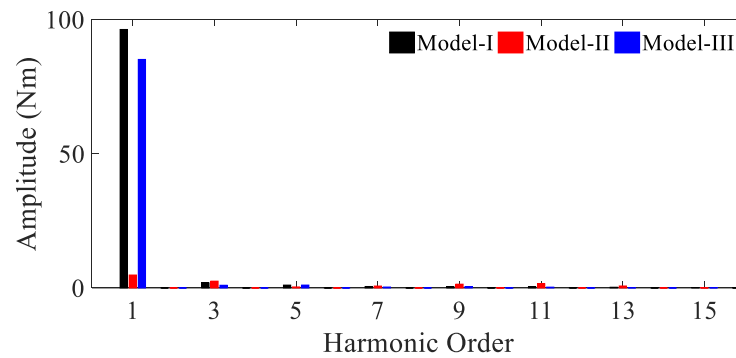
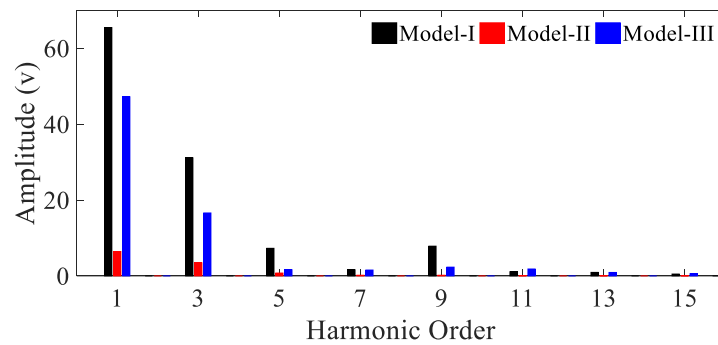


Figure 18. Torque ripple of the optimized models.



(a)



(b)

Figure 19. Optimized models: (a) Phase Back-EMF, (b) Back-EMF FFT.

It can be obtained from Figure 16a,b that the Model-II presents poor torque density. However, it produced T_{Cog} close to zero which is desirable. The Model-I provides the highest electromagnetic torque, whereas it suffers from high fluctuations in comparison with the Model-III, visiting the objective function constraints ($T_{avg} \geq 80$ Nm) with low pulsations.

Accordingly, T_{Cog} and T_{Ripple} are depicted in Figures 17 and 18 respectively, where the Model-III produced significantly low pulsations in comparison with other models and the initial $q = 2/3$ configuration, as desired in the objective function ($T_{Cog} \leq 1$ Nm and $T_{Ripple} \leq 5\%$). Meanwhile, Model-I and -II present the highest T_{Cog} and T_{Ripple} , respectively.

Figure 19a,b demonstrates the phase back-EMF and corresponding FFT analysis of the proposed models in Table 3. It can be determined that in comparison with the candidate model, the amplitude of phase back-EMF harmonics in the Model-I to -III faced a noticeable reduction. Although the phase back-EMF amplitude is low in the Model-II and -I, containing higher harmonics amplitude and even suffers from 9th harmonic order, the

Model-III produces an acceptable peak-to-peak phase back-EMF value of 67.2 V with lower amplitude harmonic orders, damped for $n \geq 5$ th harmonic.

Thus, the proposed Model-III provides the best performance and meets the established constraints, producing 85.1 Nm of torque with low pulsation, as $T_{Cog} = 0.26$ Nm and $T_{Ripple} = 1.7\%$. Flux density distribution of the optimized models are shown in Appendix A.

4.4. Efficiency and Power Factor Map

As shown in Figure 20 in terms of the efficiency map of the Model-III, considering Motoring (M) and Generating (G) modes of operation, constant torque region is provided with up to 1500 rpm of speed and with 85 Nm of torque. When in generating mode, a wider region of high efficiency is determined. Hence, constant torque above 80 Nm with an efficiency value of 80% is achievable when speed ≥ 900 rpm in M operation and speed ≥ 1100 rpm in G mode. However, efficiency $\geq 90\%$ is provided for $500 \leq \text{speed} \leq 2200$ and $500 \leq \text{speed} \leq 2500$ rpm in M and G mode respectively, producing at most 60 Nm of average torque.

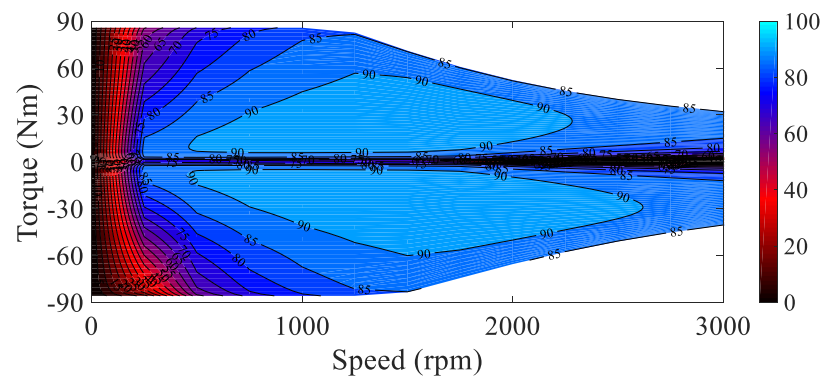


Figure 20. Efficiency (%) map of the Model-III.

Based on the Model-III power factor (PF) map illustrated in Figure 21, a higher power factor (above 0.7) is determined for $P \geq 5$ kW. As shown in Figure 21, for both M and G modes of operation, unlike the constant torque region, PF is increasing along with an increase in P for the constant power region. Conversely, in the constant torque region it declines from 0.99 to 0.7 and 0.5 in M and G mode, respectively, while in the constant power region it reaches from 0.15 to above 0.8 for both M and G operational modes.

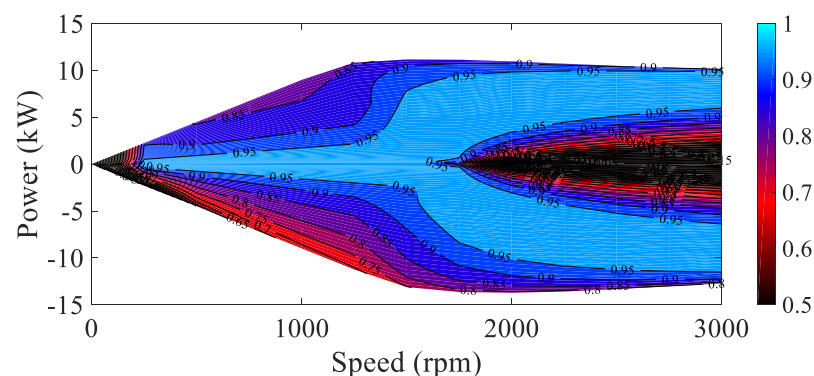


Figure 21. Power factor map of the Model-III.

Figure 22 demonstrates the corresponding phase advance (PA) analysis results for the M mode of the Model-III. Accordingly, for $0^\circ \leq PA \leq 35^\circ$ a constant torque region is provided, where speed ≤ 1500 rpm and $T_{Avg} \leq 85$ Nm. The constant power region is achieved for $35^\circ \leq PA \leq 90^\circ$ for speed values above 1500 rpm, providing average torque below 80 Nm.

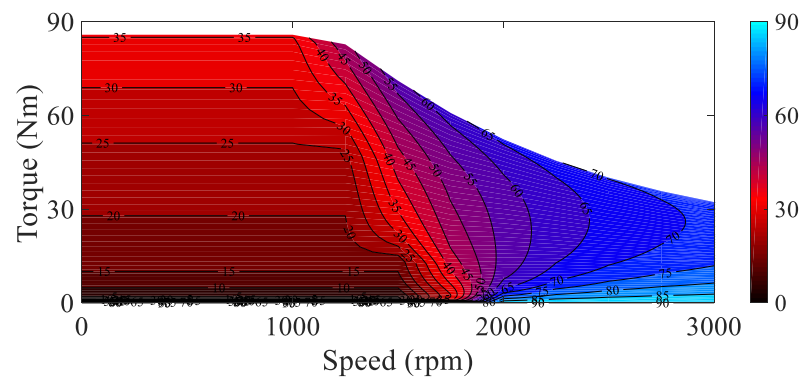


Figure 22. Phase Adv. (°) map of the Model-III.

Overall, based on the results reported, not only has the 3rd Model designed based on the optimization processes met the constraints mentioned in the objective function, but it also presents desirable torque, power, PF, and efficiency performance. These factors make Model-III the best-performed model to be adapted for an E-Motorcycle application.

4.5. Artemis Drive-Cycle Analysis

Measuring vehicle speed over time as data series in form of drive cycles (DCs) are created theoretically or based on real-world driving records. Due to developments of EV industries, DCs are mainly utilized in order to test fuel consumption and CO₂ emissions of a vehicle, and recently have begun being used to size electrical powertrain components [11].

The sizing of the powertrain is heavily dependent on vehicular and conditional parameters such as (Figure 23) [11]:

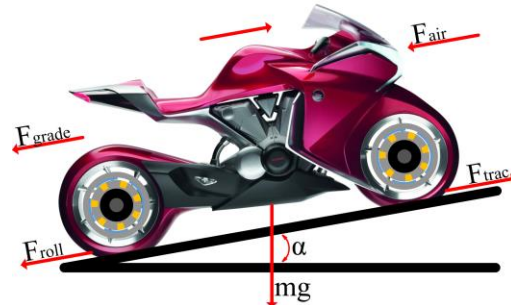


Figure 23. Dynamic traction forces of E-Motorcycle (Honda concept).

Air resistance, which is defined as F_{air} in Figure 23, representing the main force to overcome when driving on a flat road. F_{air} is proportional to air density (ρ), the square form of vehicle’s velocity (v^2), a drag coefficient (C_d) and frontal cross-sectional area of the vehicle (A):

$$F_{air} = \frac{1}{2} \rho A C_d v^2 \tag{15}$$

Rolling resistance, defined as F_{roll} , occurs due to interaction between the surface of tires and road surface. F_{roll} is proportional to vehicle mass (m), gravity acceleration (g), road gradient (α), and a rolling coefficient (C_r):

$$F_{roll} = C_r m g \cos \alpha \tag{16}$$

Grading force, F_{grade} , is the force required for up/downhill movement. F_{grade} can be either be positive or negative, thus it can be considered as resistive or supportive force and it can be determined by multiplication of m , g , and $\sin(\alpha)$:

$$F_{grade} = m g \sin \alpha \tag{17}$$

Acceleration force, F_{Acc} is a major parameter in electrical machine sizing and has a significant contribution in total traction force, calculating by-product of m and derived velocity over time (dv/dt).

$$F_{Acc} = m \frac{dv}{dt} \quad (18)$$

Traction force, F_{trac} , is the summation of the above forces in which the desired torque of the machine has a direct relation with the total traction force.

$$F_{trac} = F_{Acc} + F_{roll} + F_{grade} + F_{air} \quad (19)$$

A complete drive cycle study based on the Volvo XC90 and S60 cars can be found in [11] using a real-world database and dynamic model of the proposed cars.

Assessment and Reliability of Transport Emission Models and Inventory Systems (Artemis) is a European standard project based on a large database of European real-world driving patterns [30]. In this study, standardized Artemis DC is utilized consisting of three driving conditions:

- **Urban Cycle:** 991 s of operation with an average speed of 17.7 km/h, displacement value of 4.9 km, and Max. speed of 57.3 km/h
- **Rural Road Cycle:** 17.3 km rural road trip in 1080 s with an average speed equal to 57.5 km/h reaching its Max. at 111.1 km/h.
- **Motor Way130 Cycle:** 96.9 km/h average speed (Max. 131.4 km/h) in 1066 s for 28.75 km motorway trip.

The corresponding drive-cycle speed is illustrated in Figure 24a. For an E-Motorcycle concept design shown in Figure 23 with properties listed in Table 4, and by applying the Artemis DCs to the Model-III of this study, DC torque and DC operational data points are demonstrated in Figure 24b,c. Table 5 reports the drive cycle analysis results of each Artemis cycle applied to the Model-III.

Table 4. Drive-Cycle Properties.

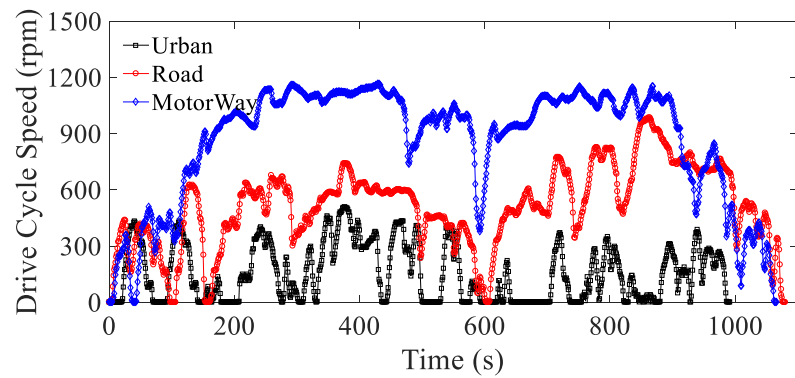
Vehicle Properties	Value
Mass (kg)	80
Rolling Resistance Coefficient	0.005
Air-Density (kg/m ³)	1.225
Frontal Area (m ²)	1.5
Drag Coefficient	0.26
Wheel Radius (m)	0.3
Mass Correction Factor	1.04
Motoring (M) Torque Ratio	1
Generating (G) Torque Ratio	1

Table 5. Artemis Drive-Cycle Data for the Model-III.

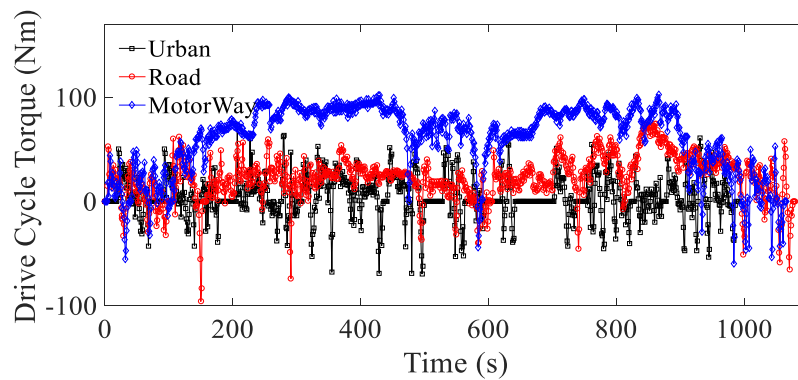
Drive Cycle	Urban	Rural	M. Way	
Data	Value	Value	Value	Unit
Time	991	1080	1066	s
Distance	4.9	17.3	28.75	km
Avg. Speed	17.7	57.5	96.9	km/h
Max. Speed	57.3	111.1	131.4	km/h
Avg. Efficiency	71.65	85.2	82.33	%
Input Energy	80.71	558.5	2291.3	Wh
Output Energy	13.53	11.4	7.54	Wh
M. Energy	60.19	478.3	1887.4	Wh
G. Energy	22.17	16.35	10.3	Wh

Table 5. Cont.

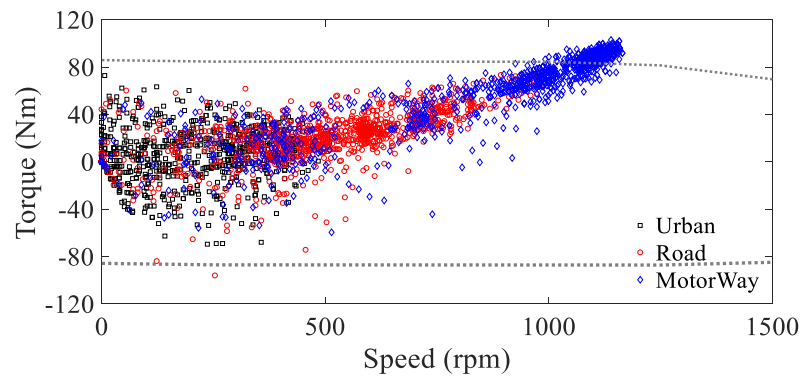
Drive Cycle	Urban	Rural	M. Way	
Data	Value	Value	Value	Unit
Total Loss	29.17	85.1	406.6	Wh
Copper Loss	24.48	66.4	369.9	Wh
Iron Loss	2.54	11.04	23.99	Wh
Magnet Loss	0	0	0.02	Wh
Mechanical Loss	2.15	7.64	12.7	Wh
M. Operation	77.8	91.2	94.5	%
G. Operation	22.2	8.8	5.53	%



(a)



(b)



(c)

Figure 24. The Artemis DC of the Model-III: (a) speed, (b) torque, and (c) operational data points under Artemis DCs.

Overall, according to Table 5, for E-Motorcycle application the studied Model-III operates efficiently with high values of torque/power density and power factor in different conditions of driving.

5. Conclusions

The goal of this paper is to investigate outer-rotor surface-mounted permanent magnet synchronous machines (OR-SPMSM) for E-Motorcycle application capable of low torque fluctuations and high torque–power density. Four winding patterns ($q = 1, 2/3, 1/2, 1/3$) are proposed and applied to the OR-SPMSM. Results are comparably reported and demonstrated that OR-SPMSM with $q = 2/3$ presents the best performance in terms of low torque pulsation. In order to investigate the advantages of this configuration and reaching enhanced design, a parameter optimization process is considered with three design parameters involved, resulting in three optimized models, producing $T_{\text{avg-Max}}$ (Model-I), $T_{\text{Cog-Min}}$ (Model-II), and $T_{\text{ripple-Min}}$ (Model-III). The results referencing each model are reported, where the Model-III provides the best performance in meeting the objective function constraints with low torque fluctuations. The Artemis Drive Cycles are applied to the Model-III in order to simulate the performance of the proposed machine for urban, road, and motorway applications of an E-Motorcycle. Accordingly, due to high torque density with low torque pulsations and efficient operation under high values of power factor, the Model-III presents the best performance and can be considered as a vital alternative for In-Wheel Light-Weight EV applications.

Author Contributions: Conceptualization, H.G. and M.M.; software, H.G. and M.M.; validation, M.M., and M.B.; writing—original draft preparation, H.G.; writing—review and editing, M.M. and M.B.; supervision, M.M. and M.B.; All authors have read and agreed to the published version of the manuscript.

Funding: This research received no external funding.

Conflicts of Interest: The authors declare no conflict of interest.

Appendix A

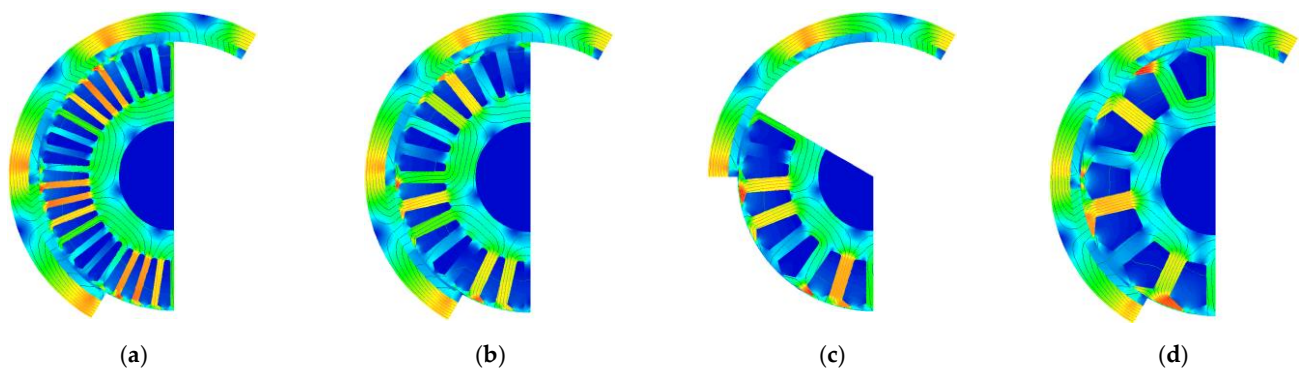


Figure A1. Flux density distribution in the initial models: (a) 42/6 and $q = 1$, (b) 28/6 and $q = 2/3$, (c) 21/6 and $q = 1/2$, (d) 14/6 and $q = 1/3$.

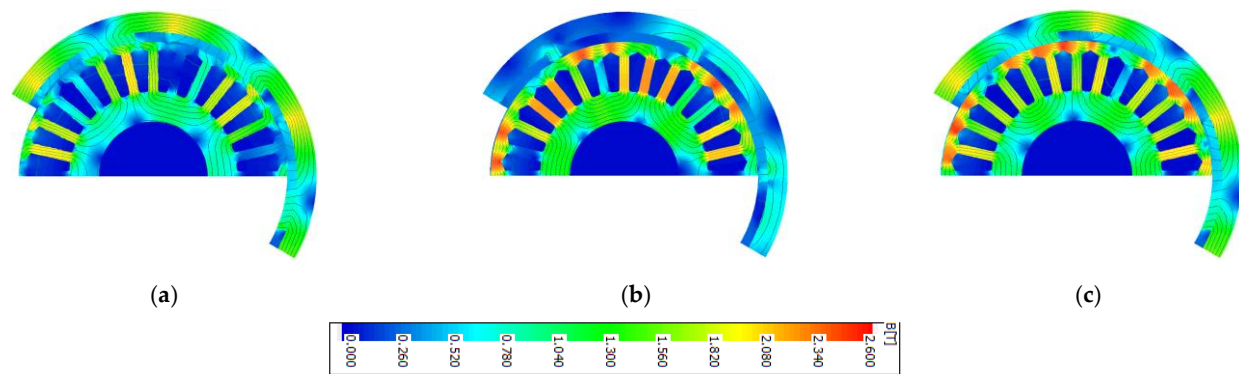


Figure A2. Flux density distribution in the optimized models: (a) Model-I, (b) Model-II, (c) Model-III.

References

- Zeraoulia, M.; Benbouzid, M.; Diallo, D. Electric Motor Drive Selection Issues for HEV Propulsion Systems: A Comparative Study. *IEEE Trans. Veh. Technol.* **2006**, *55*, 1756–1764. [\[CrossRef\]](#)
- Li, X.; Xue, Z.; Zhang, L.; Hua, W. A low-complexity three-vector-based model predictive torque control for SPMSM. *IEEE Trans. Power Electron.* **2021**, *36*, 13002–13012. [\[CrossRef\]](#)
- Marmaras, C.; Xydias, E.; Cipcigan, L. Simulation of electric vehicle driver behaviour in road transport and electric power networks. *Transp. Res. Part C Emerg. Technol.* **2017**, *80*, 239–256. [\[CrossRef\]](#)
- Ghorbani, H.R.; Moradian, M.R. Torque Pulsation Reduction in five-phase PMSyncRMs. *J. Power Electron.* **2021**, *22*, 128–137. [\[CrossRef\]](#)
- Moradian, M.R.; Soltani, J.; Najjar-Khodabakhsh, A.; Arab Markadeh, G.R. Adaptive Torque and Flux Control of Sensorless IPMSM Drive in the Stator Flux Field Oriented Reference Frame. *IEEE Trans. Ind. Inform.* **2019**, *15*, 205–212. [\[CrossRef\]](#)
- Jing, L.; Pan, Y.; Wang, T.; Qu, R.; Cheng, P.-T. Transient Analysis and Verification of a Magnetic Gear Integrated Permanent Magnet Brushless Machine with Halbach Arrays. *IEEE J. Emerg. Sel. Top. Power Electron.* **2022**, *10*, 1881–1890. [\[CrossRef\]](#)
- Jing, L.; Tang, W.; Wang, T.; Ben, T.; Qu, R. Performance Analysis of Magnetically Geared Permanent Magnet Brushless Motor for Hybrid Electric Vehicles. *IEEE Trans. Transp. Electr.* **2022**, *8*, 2874–2883. [\[CrossRef\]](#)
- Wu, D.; Fei, W.; Luk, P.C.K.; Xia, B. Design considerations of outer-rotor permanent magnet synchronous machines for in-wheel electric vehicle applications using particle swarm optimization. In Proceedings of the 7th International Conference on Power Electronics, Machines and Drives (PEMD), Manchester, UK, 8–10 April 2014. [\[CrossRef\]](#)
- Gundogdu, T.; Zhu, Z.-Q.; Mipo, J.-C. Analysis of coil pitch in induction machines for electric vehicle applications. *IET Electr. Power Appl.* **2020**, *14*, 2525–2536. [\[CrossRef\]](#)
- Tumbek, M.; Kesler, S. Design and implementation of a low power outer-rotor line-start permanent magnet synchronous motor for ultra-light electric vehicles. *Energies* **2019**, *12*, 3174. [\[CrossRef\]](#)
- Raghuraman, B.; Gyllensten, T. Electric Machine Design Based on Drive Cycle Analysis. Master's Thesis, Chalmers University of Technology, Gothenburg, Sweden, 2019.
- Ahn, J.-M.; Son, J.-C.; Lim, D.-K. Optimal design of outer-rotor surface mounted permanent magnet synchronous motor for cogging torque reduction using territory particle swarm optimization. *J. Electr. Eng. Technol.* **2021**, *16*, 429–436. [\[CrossRef\]](#)
- Fang, S.; Liu, H.; Wang, H.; Yang, H.; Lin, H. High power density PMSM with lightweight structure and high-performance soft magnetic alloy core. *IEEE Trans. Appl. Supercond.* **2019**, *29*, 0602805. [\[CrossRef\]](#)
- Ghorbani, H.R.; Majidi, B. Power Density Optimization Through Optimal Selection of PM properties in a PM-SyncRM Using FEM Analysis. In Proceedings of the 10th Annual International Power Electronics, Drive Systems and Technologies Conference (PEDSTC), Shiraz University, Shiraz, Fars, Iran, 12–14 February 2019. [\[CrossRef\]](#)
- Lee, T.-Y.; Seo, M.-K.; Kim, Y.-J.; Jung, S.-Y. Motor design and characteristics comparison of outer-rotor type BLDC motor and BLAC motor based on numerical analysis. *IEEE Trans. ASupercond.* **2016**, *26*, 5205506. [\[CrossRef\]](#)
- Zhao, J.; Zhao, S.; Yin, H.; Yang, X.; Cao, J.; Zeng, G. Design and optimization of an outer-rotor SPMSM with permanent magnets of revers step shape. In Proceedings of the 22nd International Conference on Electrical Machines and Systems (ICEMS), Harbin, China, 11–14 August 2019. [\[CrossRef\]](#)
- He, C.; Wu, T. Analysis and design of surface permanent magnet synchronous motor and generator. *CES Trans. Electr. Mach. Sys.* **2019**, *3*, 94–100. [\[CrossRef\]](#)
- Bonthu, S.S.R.; Tarek, M.T.; Choi, S. Optimal torque ripple reduction technique for outer rotor permanent magnet synchronous reluctance motors. *IEEE Trans. Energy Convers.* **2018**, *33*, 1184–1192. [\[CrossRef\]](#)
- Bonthu, S.S.R.; Choi, S.; Baek, J. Comparisons of three-phase and five-phase permanent magnet assisted synchronous reluctance motors. *IET Electr. Power Appl.* **2016**, *10*, 347–355. [\[CrossRef\]](#)
- Toliyat, H.; Waikar, S.P.; Lipo, T.A. Analysis and simulation of five-phase synchronous reluctance machines including third harmonic of airgap MMF. *IEEE Trans. Ind. Appl.* **1998**, *34*, 332–339. [\[CrossRef\]](#)

21. Toliyat, H.; Xu, L.; Lipo, T.A. A five phase reluctance motor, with high specific torque. In Proceedings of the Conference Record of the IEEE Industry Applications Society Annual Meeting, Seattle, WA, USA, 7–12 October 1990. [[CrossRef](#)]
22. Barrero, F.; Duran, J. Recent advances in the design, modelling and control of multiphase machines-Part 1. *IEEE Trans. Ind. Electr.* **2016**, *63*, 449–458. [[CrossRef](#)]
23. Scullier, F. Design of a 7-phase surface-mounted PM machine tooth-concentrated winding. In Proceedings of the XIII International Conference on Electrical Machines (ICEM), Alexandroupoli, Greece, 3–6 September 2018. [[CrossRef](#)]
24. Zhang, H.; Zhao, B.; Gong, J.; Zu, Y.; Vu, D.-T.; Nguyen, N.-K.; Semail, E.; Moraes, T.-J. Torque optimization of a seven-phase Bi-harmonic PMSM in healthy and degraded mode. In Proceedings of the 22nd International Conference on Electrical Machines and Systems (ICEMS), Harbin, China, 11–14 August 2019. [[CrossRef](#)]
25. Scullier, F.; Becker, F.; Zahr, H.; Semail, E. Design of a Bi-harmonic 7-phase PM machine with tooth-concentrated winding. *IEEE Trans. Energy Conv.* **2020**, *35*, 1567–1576. [[CrossRef](#)]
26. Ghorbani, H.; Moradian, M.; Benbouzid, M. On the Optimal Selection of Flux Barrier Reconfiguration for a Five-Phase Permanent Magnet Assisted Synchronous Reluctance Machine for Low-Torque Ripple Application. *Electronics* **2022**, *11*, 41. [[CrossRef](#)]
27. Wang, J.; Qu, R.; Zhou, L. Dual-rotor multiphase permanent magnet machine with harmonic injection to enhance torque density. *IEEE Trans. Appl. Supercond.* **2012**, *22*, 5202204. [[CrossRef](#)]
28. Jussila, H.; Salminen, P.; Niemela, M.; Pyrhonen, J. Guidelines for designing concentrated winding fractional slot permanent magnet machines. In Proceedings of the International Conference on Power Engineering, Energy and Electrical Drives, Setubal, Portugal, 12–14 April 2007. [[CrossRef](#)]
29. Martinez, D. Design of a Permanent-Magnet Synchronous Machine with Non-Overlapping Concentrated Windings for the Shell Eco Marathon Urban Prototype. Master's Thesis, Royal Institute of Technology (KTH), Stockholm, Sweden, 2012.
30. Common Artemis Driving Cycles (CADC)-Emission Test Cycles. Available online: <https://dieselnet.com/standards/cycles/artemis.php> (accessed on 1 December 2018).